AGU
ADVANCING EARTH AND SPACE SCIENCE

Earth and Space Science

Key Points:

- First observations of mesosphere and lower thermosphere dynamics over one of the most dynamically active regions in the world
- Estimates of mean horizontal winds and their gradients are possible, thanks to the multistatic configuration
- Mean momentum fluxes are estimated with vertical velocity estimates free of horizontal divergence contamination

Correspondence to:
J. F. Conte,
conte@iap-kborn.de

First Studies of Mesosphere and Lower Thermosphere Dynamics Using a Multistatic Specular Meteor Radar Network Over Southern Patagonia

J. Federico Conte[1] , Jorge L. Chau[1] , Juan M. Urco[1,2] , Ralph Latteck[1] , Juha Vierinen[3] , and Jacobo O. Salvador[4,5]

[1]Leibniz Institute of Atmospheric Physics at the University of Rostock, Kühlungsborn, Germany, [2]Department of Electrical and Computer Engineering and Coordinated Science Laboratory, University of Illinois at Urbana-Champaign, Urbana, IL, USA, [3]Arctic University of Norway, Tromsø, Norway, [4]Universidad Nacional de la Patagonia Austral, Río Gallegos, Argentina, [5]CONICET, Argentina

Abstract This paper presents for the first time results on winds, tides, gradients of horizontal winds, and momentum fluxes at mesosphere and lower thermosphere altitudes over southern Patagonia, one of the most dynamically active regions in the world. For this purpose, measurements provided by SIMONe Argentina are investigated. SIMONe Argentina is a novel multistatic specular meteor radar system that implements a Spread-spectrum Interferometric Multistatic meteor radar Observing Network (SIMONe) approach, and that has been operating since the end of September 2019. Average counts of more than 30,000 meteor detections per day result in tidal estimates with statistical uncertainties of less than 1 m/s. Thanks to the multistatic configuration, horizontal and vertical gradients of the horizontal winds are obtained, as well as vertical winds free from horizontal divergence contamination. The vertical gradients of both zonal and meridional winds exhibit strong tidal signatures. Mean momentum fluxes are estimated after removing the effects of mean winds using a 4-h, 8-km window in time and altitude, respectively. Reasonable statistical uncertainties of the momentum fluxes are obtained after applying a 28-day averaging. Therefore, the momentum flux estimates presented in this paper represent monthly mean values of waves with periods of 4 h or less, vertical wavelengths shorter than 8 km, and horizontal scales less than 400 km.

1. Introduction

The mesosphere and lower thermosphere (MLT) is the atmospheric region that couples the lower and upper parts of the terrestrial atmosphere. For this reason, knowledge of its dynamics is of great importance in order to understand the behavior of the atmosphere as a whole. The coupling is accomplished mainly via propagation of three dominant types of waves: planetary waves (PWs), tides, and gravity waves (GWs). PWs are waves with scales of thousands of kilometers and periods of up to ~30 days. They are mainly generated in the troposphere by land-sea discontinuities, or triggered in situ by, for example, baroclinic instabilities and filtered GWs (e.g., H. L. Liu & Roble, 2002; McCormack et al., 2014; Rossby, 1939). Tides are also waves with horizontal scales of thousands of kilometers, but periods that are subharmonics of the solar and lunar days. Thermal tides are mainly a consequence of solar radiation absorption by water vapor in the troposphere and ozone in the stratosphere, while the lunar tide results from the gravitational pull of the Moon (e.g., Forbes, 1984; Lindzen & Chapman, 1969). GWs are small to medium scale waves with periods ranging from about 5 min to many hours. They can be triggered by a myriad of different sources, e.g., the orography, thunderstorms, shear instabilities, convection, etc. (e.g., Fritts & Alexander, 2003; Hines, 1988; Piani et al., 2000).

During the last decades, specular meteor radars (SMRs) have been extensively used to study winds and atmospheric waves in the MLT (e.g., Clemesha et al., 2009; Hocking, 2005; Hoffmann et al., 2010; Jia et al., 2018; Laskar et al., 2016; A. Z. Liu et al., 2013, and references therein). They have also been used to study GWs, which are known to play an important role in determining the wind and thermal structure of the MLT (e.g., Fritts, 1984). Particularly, some studies have focused on extracting information about GW-driven momentum fluxes from SMR measurements (e.g., Andrioli et al., 2015; Fritts et al., 2010; Placke, Stober et al., 2011). However, understanding the results on momentum flux estimates based on SMR winds

is not trivial, mainly because of the uncertainties associated with the estimation procedure (e.g., Fritts, Janches et al., 2012). In fact, Vincent et al. (2010) showed that the accuracy in the momentum flux estimation is highly dependent on the number of meteor detections. Consequently, the usage of multistatic meteor radar systems represents one way to reduce the uncertainties of the momentum flux estimates (e.g., Spargo et al., 2019). Furthermore, by detecting more meteors and being able to observe them from different viewing points, multistatic SMR systems also allow for more reliable estimations of horizontal wind gradients.

The MLT over the southern part of Argentina and Chile is considered to be one of the most dynamically active regions in the globe. Satellite-based studies have revealed that GW-driven momentum fluxes increase considerably at both stratosphere and MLT altitudes over Patagonia (e.g., Trinh et al., 2018; Vadas et al., 2019). Numerical model simulations have reported generation of secondary GWs with horizontal scales of up to 2,000 km at mesospheric altitudes over the southern Andes (Vadas & Becker, 2019). Nevertheless, wave coupling processes in the MLT region over the Patagonian sector are still not well understood, partly because the installation of ground-based instruments has not been possible, either due to logistics challenges or instrument requirements. In this work, we present preliminary results of a multistatic SMR network that allows, for the first time, measurements of MLT dynamics in the Patagonian region. Besides the local support, our success has been possible thanks to a novel approach that we call Spread Spectrum Interferometric Multistatic meteor radar Observing Network (SIMONe; Chau et al., 2019). SIMONe makes use of modern radar practices like spread-spectrum, MIMO (multiple-input, multiple-output), and compressed sensing applied to atmospheric radars (Urco et al., 2018, 2019; Vierinen et al., 2016). This allows for much easier installation, operation, and expansion of the network than previous equivalent systems.

The paper is organized as follows. Section 2 introduces the SIMONe Argentina system. Section 3 provides a detailed description of the different analyses performed to the data. The main results and findings are presented and discussed in Section 4. Finally, the concluding remarks are provided in Section 5.

2. SIMONe Argentina

SIMONe Argentina is a state-of-the-art network of multistatic SMRs that was installed in September of 2019 in the southern province of Santa Cruz, Argentina. It is comprised of one single transmitting site with five linearly polarized Yagi antennas in a pentagon configuration, and five receiving sites with one dual-polarization Yagi antenna each. The receivers are placed between 30 and 270 km of distance from the transmitting site, which is located at 49.6°S, 71.4°W (see Figure 1 for details on the geographical distribution of the sites). This type of network configuration is known as MISO (multiple-input, single-output), since only one antenna is used on reception (e.g., Chau et al., 2019).

SIMONe Argentina is the result of an effort led by the Leibniz Institute of Atmospheric Physics (Germany) in collaboration with the Universidad Nacional de la Patagonia Austral (Argentina), and the Arctic University of Norway. A similar system has been installed in Peru (SIMONe Peru). SIMONe systems use coded spread spectrum on transmission (Vierinen et al., 2016). A phase coded signal based on pseudorandom sequences is generated and transmitted on each antenna independently. Transmission is done at a frequency of 32.55 MHz and with an average power of 400 W per antenna. All five transmitted codes are simultaneously decoded at each receiving site by means of compressed sensing (e.g., Urco et al., 2019). Hardware and software details of both systems, that is, SIMONe Peru and SIMONe Argentina, can be found in Chau et al. (2020).

SIMONe Argentina started operations by the end of September 2019 and has been running since then with almost no interruptions. Figure 2 shows a summary of the detection statistics for the first 7 months of operations. The upper panel indicates the normalized percentage of meteor counts for each individual link. The bottom panel is used to present the average daily total counts for each month. Problems with the local power supply at the transmitting site resulted in fewer meteor detections during April of 2020. Besides, the receiving site at Gobernador Gregores was out of operation during December of 2019 due to damage in the antenna cables. Nevertheless, for most of the time, the number of counts was much higher than in standard SMRs. The links concentrating most of the meteor detections are Tres Lagos-El Calafate and Tres Lagos-La Estela. Starting in March 2020, the link Tres Lagos-Rio Gallegos exhibits a considerable increase in the counts, as a result of having rotated the transmitting antennas by 90°. By month, January presents the largest counts, with an average of more than 50,000 meteor detections per day.
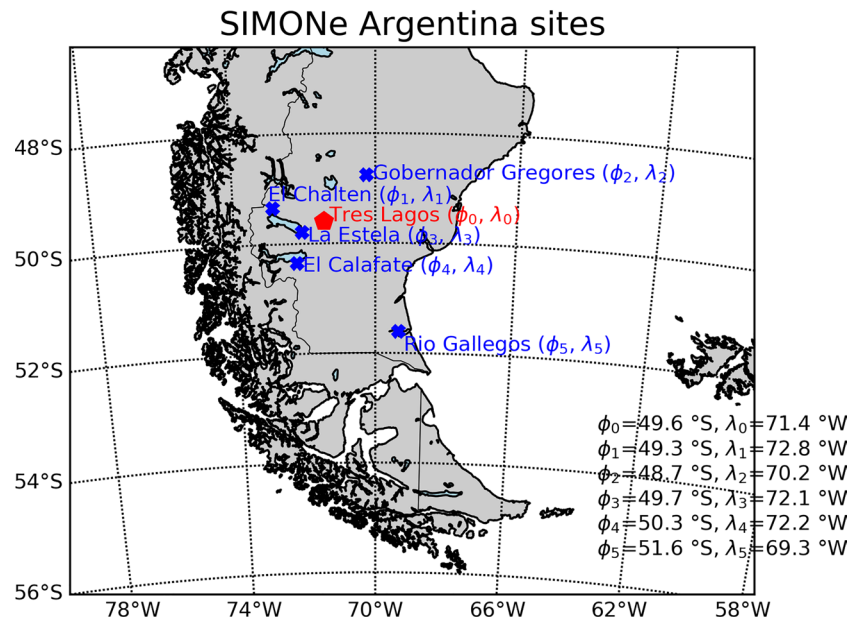
Figure 1. Map of SIMONe Argentina. The transmitter is indicated with a filled red pentagon, and the receivers are indicated with blue crosses.

3. Data Analysis

SMRs are used to measure the Doppler shift of meteor trails due to their drifting with the mesospheric neutral winds (e.g., Jones et al., 1998). In order to extract the wind information from the measurements, one may implement an all-sky fit of the Doppler velocities measured during a certain period of time and within a given altitude interval (e.g., Hocking et al., 2001; Holdsworth et al., 2004). In other words, one must solve the following equation:
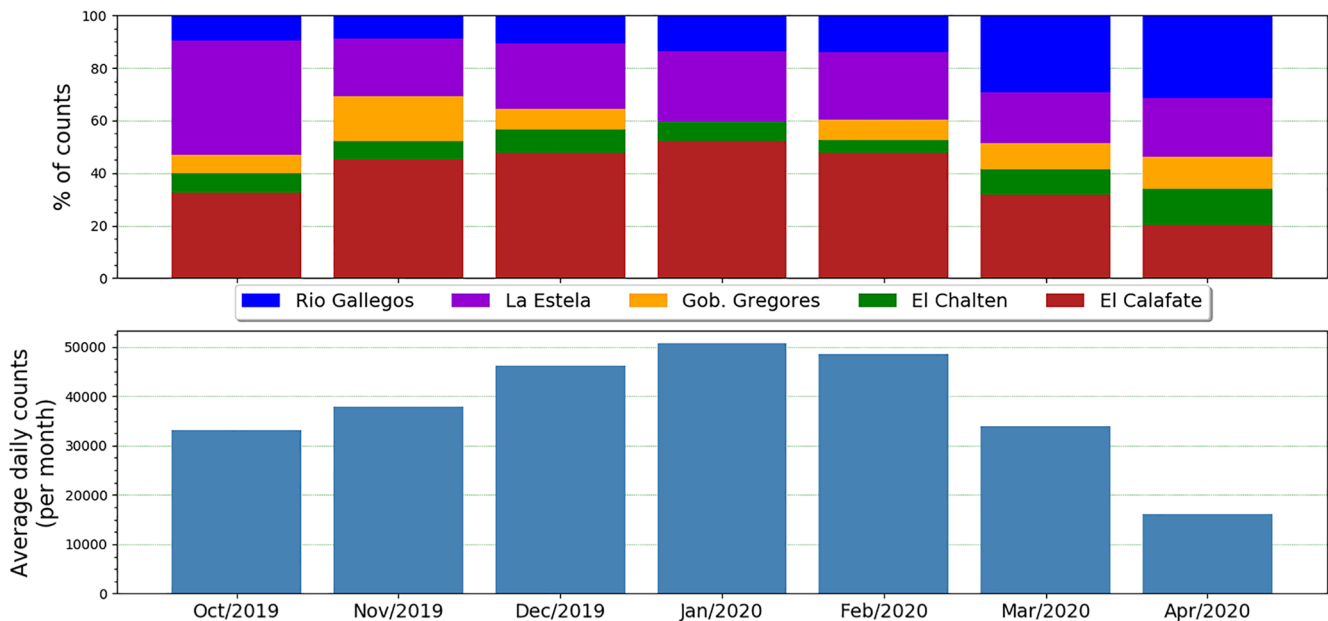

Figure 2. Upper panel: normalized percentage of meteor counts, color coded for each individual link. Bottom panel: monthly daily mean counts for all the links combined (see text for details).

$$\mathbf{u} \cdot \mathbf{k} = 2\pi f + \zeta, \tag{1}$$

where $\mathbf{u} = (u, v, w)$ is the neutral wind vector, with u, v, and w being its zonal (east-west), meridional (north-south), and vertical (up-down) components, respectively. $\mathbf{k} = (k_u, k_v, k_w)$ is the Bragg wave vector (scattered minus incident) in the meteor-centered east-north-up coordinate system (perpendicular to the meteor trail); f is the Doppler shift; and ζ is the Doppler shift uncertainty. For this equation to be valid, one must make the assumption that the winds at each given height interval are uniform during the selected period of time (homogeneous method). The results using the homogeneous method have been obtained assuming $w = 0$.

Monostatic SMRs commonly allow for hourly horizontal wind estimations every 2–3 km in altitude (e.g., Hoffmann et al., 2010; Jacobi et al., 1999). The wind estimates are representative of mean values over an area of ~200 km in radius. These horizontal winds can be further processed in order to obtain information about large scale waves such as PWs and tides (e.g., Chau et al., 2015; Conte et al., 2018; Murphy et al., 2006).

One of the advantages of using multistatic SMR networks is that the amount of meteor detections is significantly increased (e.g., Stober & Chau, 2015). During most of the time since it started operations, SIMONe Argentina has been capable of detecting more than 30,000 meteors per day (see Figure 2). With such amounts of meteor detections, one can not only reliably estimate horizontal winds with higher time and vertical resolutions (~15 min and 1 km, respectively), but also investigate second-order parameters such as the squares of the perturbation components of the radial velocities, that is, the momentum flux components (e.g., Spargo et al., 2019). Another advantage multistatic SMR networks present is that they are capable of sampling the observed volume from different viewing angles. In this scenario, the increased number of meteor detections can be further exploited in order to estimate first-order derivatives of the horizontal winds, and in this way include in the estimation a mean vertical wind free of horizontal divergence contamination (e.g., Chau et al., 2017).

Below, we describe the main procedures used in this work, that is, tidal estimation, wind estimation using a gradient method, and mean momentum flux estimation. For each of the three procedures, a first wind estimation is carried out in order to remove outliers. That is, Equation 1 is solved in bins of the same size as that used later on in each given procedure (e.g., 4 h, 4 km in the gradient method); and then the radial velocities the values of which have a corresponding residual of more than 3 standard deviations are removed. This first wind estimation is carried out only in those bins containing a minimum of 10 meteor detections.

3.1. Tidal Estimation

Horizontal winds obtained from meteor radar measurements have been used for several decades to investigate tides and PWs in the MLT (e.g., Fritts, Iimura et al., 2012; Hocking & Thayaparan, 1997). Different mathematical techniques such as least squares or wavelet analysis can be applied to the wind data in order to extract the tidal information (e.g., He et al., 2017; Sandford et al., 2006; Stening et al., 1997). To avoid zero-padding or interpolating when encountering data gaps, a least squares approach was selected for this study.

After removing the outliers, Equation 1 was again fitted to the Doppler shift measurements. For this purpose, a weighted least squares (WLS) technique was implemented using bins of 1 h and 2 km (in altitude), shifted by half an hour and 1 km, respectively. The inverse of the squared Doppler shift uncertainties (ζ in Equation 1) were used as weights. The WLS was carried out only in those bins containing a minimum of 10 meteor detections. Then, under the assumption that the obtained hourly horizontal winds are the result of the superposition of a mean wind and different period oscillations, the following equation was fitted to the zonal (u) and meridional (v) wind components

$$\left[u + \psi_u, v + \psi_v\right] = \left[U_0, V_0\right] + \sum_{i=1}^{4} \left[A_u, A_v\right]_i \cos\left(2\pi \frac{\left(t - \left[\phi_u, \phi_v\right]_i\right)}{T_i}\right). \tag{2}$$

Here, ψ_u and ψ_v are the Doppler shift uncertainties (error) propagated into the estimated winds; U_0 and V_0 are the mean zonal and meridional winds; A_{u_i} (A_{v_i}) and ϕ_{u_i} (ϕ_{v_i}) are the amplitude and phase, respectively,

of the zonal (meridional) component of each considered wave; $T_1 = 2$ days; T_i for $i > 1$ is the period of each considered tide ($T_2 = 24$ h, $T_3 = 12$ h, and $T_4 = 8$ h, for the diurnal, semidiurnal, and terdiurnal solar tides, respectively); and t is the Universal Time (UT) in hours. The cosine of a sum was used to linearize Equation 2, which then was solved by applying the WLS method using a running window of 4 days shifted by 1 day.

3.2. Wind Field Gradient Method

If one relaxes the assumption of homogeneity, the wind field inside the observed area may be estimated using the gradient method. This method consists in approximating the horizontal winds with their first-order Taylor expansion terms (e.g., Browning & Wexler, 1968; Burnside et al., 1981; Chau et al., 2017). This means introducing the following expression into Equation 1

$$\mathbf{u}(x,y,z,t) = \mathbf{u}_0(z,t) + \mathbf{u}_x(z,t)(x - x_0) + \mathbf{u}_y(z,t)(y - y_0) + \mathbf{u}_z(z,t)(z - z_0),$$ (3)

where $\mathbf{u}_0 = (u_0, v_0, w_0)$ represents the mean wind; $\mathbf{x}_0 = (x_0, y_0, z_0)$ is a reference point; and

$$\mathbf{u}_x = \left(\frac{\partial u}{\partial x}, \frac{\partial v}{\partial x}, \frac{\partial w}{\partial x} \right)$$

$$\mathbf{u}_y = \left(\frac{\partial u}{\partial y}, \frac{\partial v}{\partial y}, \frac{\partial w}{\partial y} \right)$$

$$\mathbf{u}_z = \left(\frac{\partial u}{\partial z}, \frac{\partial v}{\partial z}, \frac{\partial w}{\partial z} \right).$$

The mean wind and the first-order derivatives depend only on time and height. The coordinates (x, y, z) are in km, and calculated taking into consideration the latitude, longitude and altitude of each meteor detection and the radius of the Earth at the reference point. $\mathbf{x}_0$ is determined using the latitude and longitude of the transmitting site, and the altitude of each height level considered in the WLS fit. The latter was implemented using bins of 4 h and 4 km (in altitude), shifted by 15 min and 1 km, respectively. For this study, we have assumed that $(\partial w/\partial x, \partial w/\partial y, \partial w/\partial z) = \mathbf{0}$, which means solving for nine unknowns. In this method, a condition of having a minimum of 40 meteor detections per bin was selected.

Mathematically speaking, the zero-order approximation ($\mathbf{u}_0$) as well as the first-order derivatives ($\mathbf{u}_x$, $\mathbf{u}_y$, and $\mathbf{u}_z$) are defined at the reference point, $\mathbf{x}_0$. However, the dependence of our nine estimates on this reference point is not explicitly written in Equation 3 for the following reason. The mean winds and the gradients are obtained after fitting measurements made at points randomly distributed within an area of roughly $\sim$200 km of radius around $\mathbf{x}_0$. Thus, it is assumed that they represent a "mean" zero-order approximation, and "mean" first-order derivatives, not only at the reference point, but over the whole area aforementioned.

3.3. Momentum Flux Estimates

The procedure followed in this study to estimate the GW momentum flux is based on the works by Thorsen et al. (1997) and Hocking (2005). It consists in applying a least squares method to solve the following equation

$$(\mathbf{u}' \cdot \mathbf{k})^2 = (2\pi(f - \hat{f}))^2.$$ (4)

In this expression, $\mathbf{k}$ and f are, respectively, the same Bragg wave vector and same Doppler shift as in Equation 1, but $\mathbf{u}'$ represents the perturbed wind vector instead. $\hat{f}$ is a so-called mean Doppler shift,

$$\hat{f} = \mathbf{u} \cdot \mathbf{k} / 2\pi,$$ (5)
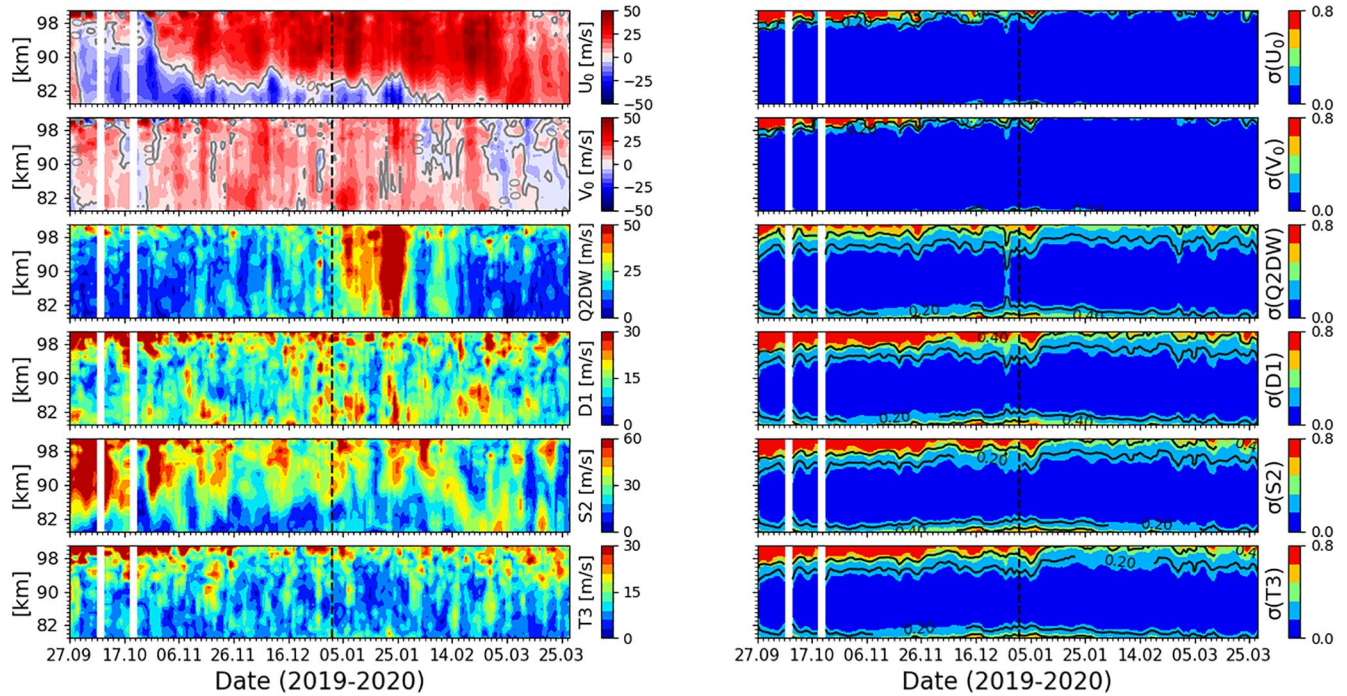
SIMONe Argentina - Mean winds & tides

Figure 3. Mean zonal (U_0) and meridional (V_0) winds, the quasi 2-day planetary wave (Q2DW), and the diurnal (D1), semidiurnal (S2) and terdiurnal (T3) solar tides during September 2019–April 2020 over SIMONe Argentina. The corresponding statistical uncertainties (in m/s) are shown in the right column. All parameters were estimated using a 4-day running window shifted by 1 day. The vertical black dashed line indicates January 1, 2020.

where **u** is the mean wind that results from solving Equation 1 or 3. To guarantee more reliable values of the six unknowns (<u'u'>, <v'v'>, <u'w'>, <v'w'>, <u'v'> and <w'w'>), the fit was performed only in those bins containing 40 meteor detections or more.

From Equations 4 and 5, it follows that different momentum flux estimates may be obtained depending on the mean wind that is used to determine $\hat{f}$. In this study, the wind estimates that result from applying the gradient method were used to calculate $\hat{f}$ (see previous section). That is, Equation 3 (with $\partial w/\partial x = \partial w/\partial y = \partial w/\partial z = 0$) was introduced into Equation 1, and the latter then solved using bins of 4 h and 8 km, shifted by 15 min in time and 1 km in altitude. Finally, Equation 4 was solved in bins of 4 h and 4 km (in altitude), shifted by 30 min and 1 km, respectively.

4. Results and Discussion

One of the main goals of this work is to provide, for the first time, information on the MLT dynamics over southern Patagonia obtained using SIMONe Argentina. For this reason, our results are discussed as they are presented.

4.1. Mean Winds and Tides

In Figure 3, we present the mean zonal (U_0) and meridional (V_0) winds, and the total amplitudes of the quasi 2-day planetary wave (Q2DW) and the diurnal (D1), semidiurnal (S2) and terdiurnal (T3) solar tides. The vertical black dashed line indicates January 1, 2020. The term *total amplitude* refers to the magnitude of the vector sum of the corresponding zonal and meridional components of each fitted wave. The statis-

tical uncertainties of the estimated parameters are shown in the right column panels. All quantities were obtained after applying the procedure detailed in Section 3.1. Data gaps are shown in white.

From inspection of Figure 3, two features stand out: the S2 tide is the dominant wave, with amplitudes in the order of 40–65 m/s, and the Q2DW exhibits strong enhancements after January 4, 2020. It is well-known that the semidiurnal solar tide at middle latitudes dominates over all other tidal components (e.g., Andrews et al., 1987; Pancheva & Mukhtarov, 2011). Furthermore, many studies of tides in the northern hemisphere have reported that S2 decreases significantly around the onset of a sudden stratospheric warming (SSW) event, to later on recover and reach even larger amplitudes than those exhibited prior to the SSW (e.g., Chau et al., 2015; Conte et al., 2019; Siddiqui et al., 2018). In September of 2019, ~12 days before the 27th (first day of available data from SIMONe Argentina), a SSW event was registered in the Southern Hemisphere (e.g., Yamazaki et al., 2020). Interestingly enough, the largest amplitudes of S2 are seen between September 27 and October 12, which may be an indicative of the recovery phase of S2 after the weakening associated with a SSW event. On the other hand, it is also possible that the reported enhancement of S2 is simply the result of changes in the propagation conditions of this tidal component. For example, the S2 amplitudes may change due to different responses of the symmetric and antisymmetric Hough modes to the weaker and more hemispherically symmetric mean zonal wind typical of the equinox times. Previous studies of the S2 tide at middle latitudes of the Southern Hemisphere have shown a decrease of S2 in the beginning of September, and a later recovery by the beginning of October (e.g., Conte et al., 2017). However, this decrease/increase behavior of S2 during the September-October months is not obvious every year. Finally, note that for the entire data set analyzed in this study, S2 presents significant intraseasonal variability, which becomes evident in the many, although weaker, enhancements observed after ~October 31.

The Q2DW at middle latitudes has been reported to reach maximum amplitudes during the summer (e.g., Kumar et al., 2018). In our results, the Q2DW is active mostly in summer, in agreement with previous studies. Even more, it becomes the dominant wave by the end of January 2020, with amplitudes larger than those corresponding to S2. Offermann et al. (2011) showed that the Q2DW exhibits a triple-peak structure in the NH during summer. Although it may not be obvious at first, after a more through inspection of Figure 3, it can be noticed that the largest amplitudes of the Q2DW are distributed in three subsequent enhancements, around January 7, 13, and 19. A fourth enhancement can be seen around February 9, but the latter is significantly weaker than the previous three.

Both the diurnal and terdiurnal solar tides exhibit considerable intraseasonal variability. In the case of D1, its activity becomes more evident mostly below ~90 km and during summer. Above ~92 km, and mainly during equinox times, T3 becomes more noticeable, with amplitudes similar to those corresponding to D1.

Compared to 5-year average values at 54°S presented by Conte et al. (2017), the summer reversal of the mean zonal wind shown in Figure 3 is observed at altitudes ~2 km lower. This is consistent with previous studies reporting a decrease with latitude of the height of the zonal wind summer reversal (e.g., Hoffmann et al., 2010; Wilhelm et al., 2019). Besides, it might seem that U_0 starts the transition into summer conditions relatively early, around October 3. However, above ~92 km, U_0 experiences a late reversal to westward conditions around October 24, to finally go into summer conditions (i.e., eastward above the mesopause) about 5 days later. V_0 blows mainly toward the equator, and only after March 10, poleward values start to dominate.

The statistical uncertainties of all the fitted parameters presented in Figure 3 are very small. Only above 103 km and below 77 km, values of ~2–3 m/s are obtained (not shown). The low statistical uncertainties are a consequence of the large amount of meteor detections provided by SIMONe Argentina. By solving Equation 1 in bins of 1 h and 2 km, one guarantees wind estimates with very low uncertainties. The latter, combined with the fact the WLS method used to solve Equation 2 is applied to a very well-conditioned matrix, results in small statistical uncertainties.

4.2. Gradients and Vertical Wind

In Figure 4, we present one week of 4-h, 4-km mean winds and gradients obtained after applying the procedure described in Section 3.2. The first row shows, from left to right, the mean zonal (u_0), meridional (v_0),
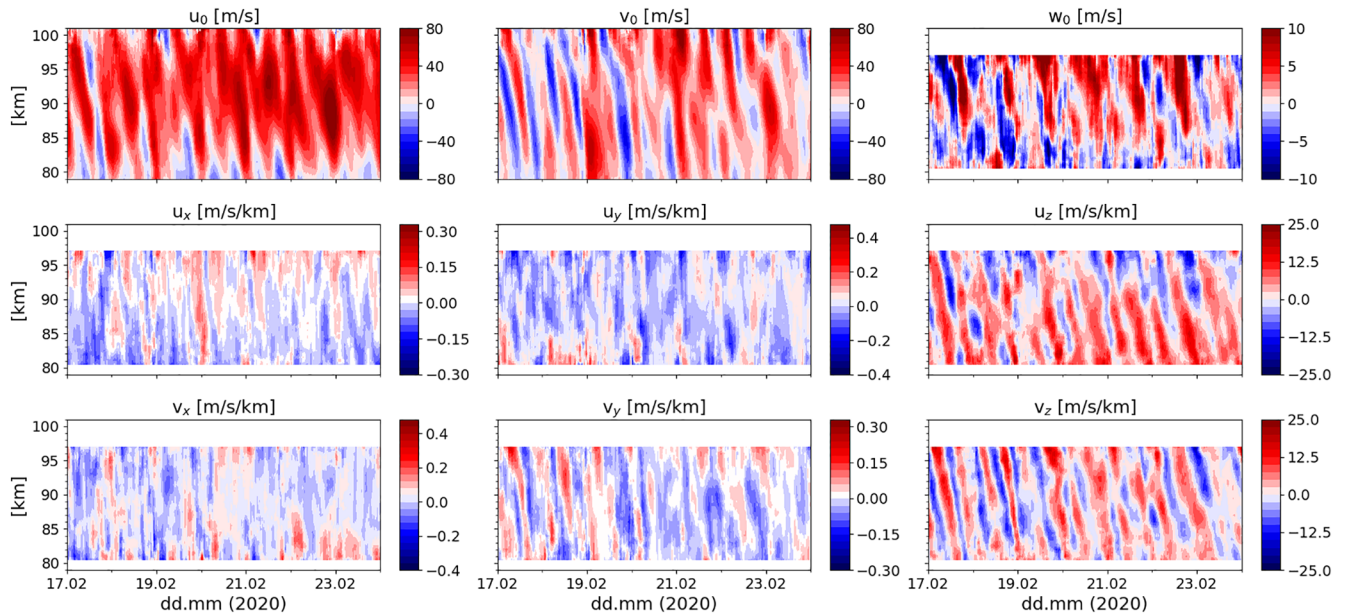
Figure 4. SIMONe Argentina estimates of: (first row) mean zonal (u_0), meridional (v_0) and vertical (w_0) winds; (second row) zonal eastward (u_x), meridional (u_y) and upward (u_z) derivatives; (third row) meridional eastward (v_x), northward (v_y) and upward (v_z) derivatives. All parameters were estimated using a 4 h, 4 km (in vertical) bin, shifted by 15 min and 1 km, respectively.

and vertical (w_0) winds. The panels in the middle row are used to show the zonal eastward, northward, and upward (first-order) derivatives, that is, u_x, u_y, and u_z, respectively. The bottom row shows the same as the middle one, but for the meridional component, that is, v_x, v_y, and v_z. The mean winds are given in m/s, and the gradients in m/s/km. The mean vertical wind and the gradients are shown only between 80 and 97 km of altitude, where the data coverage is good enough to estimate them more reliably.

Before starting the description of the main features observed in Figure 4, it is important to stress here that the variability seen in the mean winds is representative of large scale structures, with periods greater than 4 h and vertical wavelengths larger than 4 km. Both u_0 and v_0 exhibit a clear diurnal and semidiurnal periodicity, the latter being more evident, something expected given the latitude of SIMONe Argentina. The semidiurnal periodicity is also very clear in the vertical gradients, u_z and v_z, which indicates a strong influence of the S2 tide in the vertical changes of the horizontal winds. Although they may not be evident in Figure 4, other periodicities are present in the vertical gradients. For example, GW effects can be noticed below 90 km. At these altitudes, u_z is mainly positive (with mean values in the order of 20 m/s/km). In fact, during most of the summertime, below ~90 km of altitude, and when averaged over longer periods of time, for example, 1 day, u_z is strongly dominated by positive amplitudes (not shown here). During the summer, westward zonal winds are dominant in the stratosphere and mesosphere. This condition allows eastward propagating GWs to easily reach mesospheric altitudes, where they break and deposit momentum and energy. This deposition of momentum creates an eastward drag that decelerates the zonal (westward) wind. Due to the Coriolis effect, the deceleration of the zonal wind introduces an equatorward meridional wind component, which in turn leads to an upward motion and a subsequent (adiabatic) cooling of the mesopause region (e.g., Smith, 2012). Finally, due to the thermal wind equation, $u_z \approx -\alpha(\phi)\partial T/\partial y$ (where y is positive toward north, T is the temperature, and α is a factor that depends on the sine of the latitude, ϕ), the adiabatic cooling results in the positive values of u_z. In the case of v_z, the amplitudes are in the order of 3–5 m/s/km weaker than those of u_z, but the semidiurnal periodicity is seen at all altitudes. No evident pattern or structure in time can be noticed when v_z is averaged over longer periods of time.

In the case of u_x and v_x, amplitude values are in the order of 0.1–0.3 m/s/km. The larger amplitudes of u_y (compared to u_x) may be an indicative of zonal wind latitudinal changes related to the Antarctic polar vortex,

part of which may locate below the region seen by SIMONe Argentina (e.g., Figure 8 in Orte et al. [2019]). The upward component of the relative vorticity can be coarsely approximated by $v_x - u_y$ (for a precise calculation, one needs to include the latitude information; see Equation A16 in Chau et al. [2017]). Below $\sim$84 km, $v_x - u_y$ values are mainly positive, which suggests counterclockwise vortical effects. Besides, differences between the amplitudes of u_y, v_x and u_x, v_y, suggest that changes in the horizontal gradients due to GWs depend on the propagation direction of these waves.

The errors in both the horizontal and vertical gradients are in the order of 5%–10%. For example, for the week of data shown in Figure 4, the root mean square errors of u_x, u_y, u_z, v_x, v_y, and v_z are 0.011, 0.023, 1.1, 0.022, 0.013, and 0.99 m/s/km, respectively.

Previous observational studies have investigated the horizontal gradients in the zonal and meridional winds (e.g., Chau et al., 2017; Conde & Smith, 1998; Meriwether et al., 2008). However, the present study is the first one to show results on both the horizontal and vertical gradients of MLT horizontal winds over southern Patagonia. Chau et al. (2017) showed that horizontal divergence values of $\sim$0.1 m/s/km are large enough to introduce a mean apparent vertical wind of 1–2 m/s. After calculating $u_x + v_y$, one obtains values in the order of 0.4–0.5 m/s/km. Consequently, one can now understand the importance of estimating the vertical wind together with the gradients. By doing so, one eliminates the effects of biases introduced in w_0 by the mean horizontal variability of u and v. However, the horizontal variability within scales smaller than the observed volume is not removed, and will affect the vertical wind estimates.

The 4-h mean vertical winds (w_0) exhibit large amplitudes and considerable variability both in time and height. The errors in these estimates are in the order of 1–2 m/s. After computing daily averages, vertical wind amplitudes are reduced to a few m/s, which are still considerably large values. Previous studies have investigated MLT mean vertical winds using SMRs. For example, Babu et al. (2012) and Egito et al. (2016) reported that the vertical winds at low latitudes may reach magnitudes of 6–10 m/s. Using VHF radar measurements, Fritts et al. (1990) observed that at summer mesopause altitudes vertical velocities may reach values of up to 10 m/s, but within time scales of 5–30 min. That is, vertical winds should exhibit values in the order of a few to tens cm/s when averaged over periods of 1 day or more (e.g., Lu et al., 2017).

There are several factors that adversely affect our vertical wind estimates. (1) The daily variability in the meteor counts (meteor detections maximize early in the morning and minimize in the evening) can result in irregular time sampling at altitudes where the detections are lower, that is, above 97 km and below 80 km, in the case of SIMONe Argentina. For this reason, we have limited our analysis of w_0 to altitudes between 80 and 97 km. (2) Despite the multistatic configuration, sometimes the meteor detections are not well distributed among all five links. This affects in a similar way every altitude observed by SIMONe Argentina. (3) Small-scale horizontal variability is not removed after applying the gradient method. Hence, horizontal changes of the zonal and meridional winds occurring within the observed volume can easily leak into the vertical winds, and thus result in the large w_0 values presented in Figure 4. To better understand and quantify the adverse impact of points (2) and (3), we are currently working in applying the gradient method to forward modeled data using different geometric configurations. This will shed light on the reliability of the vertical winds presented in this study as well as other studies using multistatic SMR configurations.

Despite the large amplitudes, coherent phase structures can be seen in w_0. For example, around February 17, one can observe a clear diurnal periodicity. Diurnal wave signatures in w_0 have been found throughout the entire SIMONe Argentina data set (not shown). Moreover, similar features have been observed in the mean vertical winds over Peru and northern Germany (Charuvil Asokan et al., 2020; Chau et al., 2020). Hence, it is possible that our results on w_0 are also revealing real geophysical features, for example, diurnal tidal effects. However, it is necessary to mention that currently we cannot rule out the possibility that such tidal signatures are due to leakage from the small-scale horizontal variability of u and v. This will be carefully investigated in future studies.

4.3. Gravity-Wave-Driven Momentum Flux

We now present and discuss the momentum flux estimates obtained after subtracting the mean winds calculated following the gradient method, that is, the u_0, v_0, and w_0 that were estimated together with the
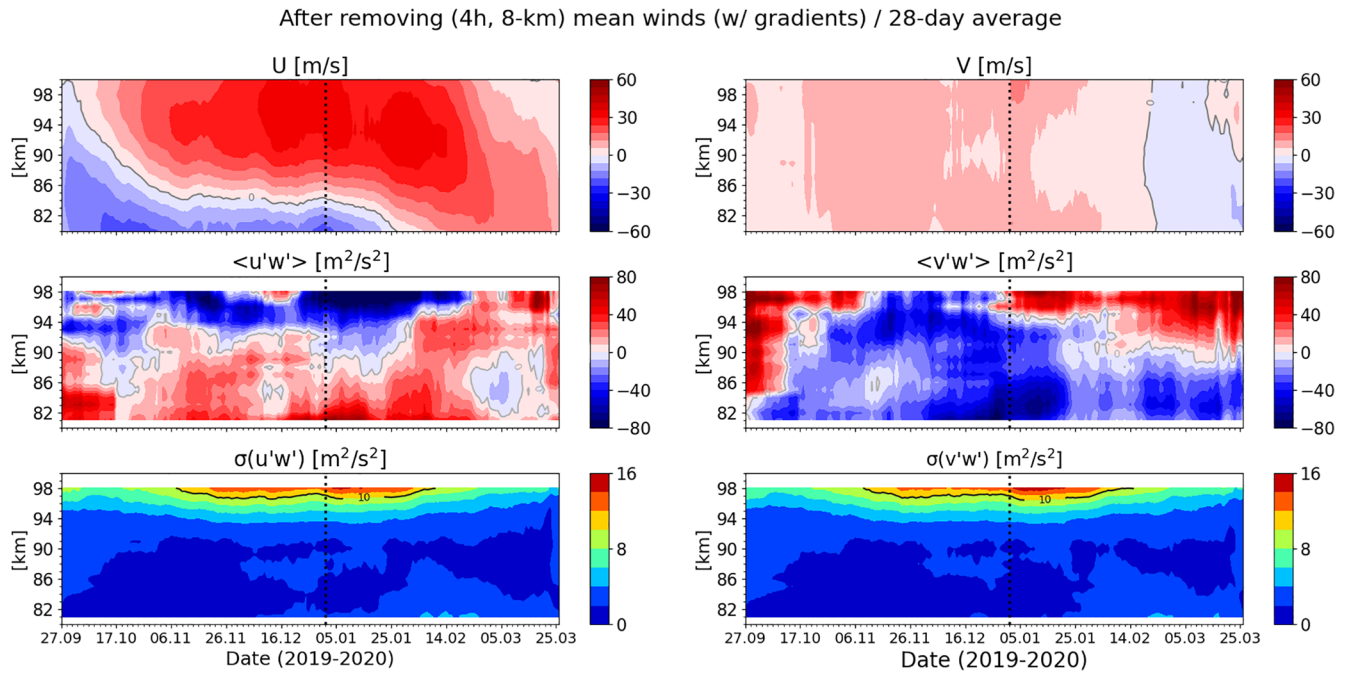
Figure 5. Twenty-eight-day averages of 4-h, 8-km mean zonal and meridional winds (U and V, respectively), horizontal momentum vertical fluxes (<u'w'>, <v'w'>) and their corresponding statistical uncertainties (σ(u'w'), σ(v'w')). 4 h, 8 km (in altitude) mean horizontal and vertical winds estimated in combination with the gradients (i.e., the u_0, v_0, w_0 described in Section 3.2) were subtracted before estimating the momentum flux. The vertical black dashed line indicates January 1, 2020.

gradients. In Figure 4, it can be seen that the horizontal wind gradients and the vertical mean wind exhibit considerable variability, both in time and altitude. Part of this variability is leaked into the mean horizontal winds when one solves Equation 1 without including the gradients and w_0 in the wind vector **u**. This implies that the u_0 and v_0 obtained using the gradient method constitute a better representation of the real mean wind, provided that enough meteors are detected in order to accomplish a robust wind estimation. Besides, it is important to have in mind that the subtracted winds were estimated in bins of 4 h and 8 km (in altitude). This means that the corresponding momentum flux estimates are representative mostly of waves with temporal and vertical scales of less than 4 h and 8 km, respectively.

In Figure 5, we present 28-day averages of the momentum flux estimates that result from subtracting the $\hat{f}$ that was calculated using the u_0, v_0, w_0 mentioned in the previous paragraph (see Equation 4). The averages were calculated over 28 days in order to obtain estimates that are statistically more significant. The upper panels present *U* and *V*, which correspond to the 28-day averages of the mean zonal and meridional winds, respectively. The middle panels are used to show the 28-day mean horizontal momentum vertical fluxes, <u'w'>, <v'w'>. The statistical uncertainties of <u'w'> and <v'w'>, that is, σ(u'w') and σ(v'w'), respectively, are shown in the bottom panels.

Momentum flux estimations based on SMR observations were first presented by Hocking (2005). Since then, several studies have investigated momentum fluxes using meteor radar winds (e.g., Andrioli et al., 2013; Fritts et al., 2010; Fritts, Janches et al., 2012; Placke, Hoffmann et al., 2011; Placke et al., 2015, and references therein). More recently, de Wit et al. (2016) observed a modulation by the quasi-biennial oscillation of the momentum fluxes over Tierra del Fuego, an island south of Santa Cruz province. Typical amplitudes of <u'w'> and <v'w'> reported in these previous studies rarely reach values larger than 60–70 m^2/s^2. Using a multistatic meteor radar network over southern Australia, Spargo et al. (2019) observed values for <u'w'> and <v'w'> in the order of 40–60 m^2/s^2, which are larger than momentum flux absolute values obtained from satellite measurements (e.g., Ern et al., 2011; Trinh et al., 2018). The latter is most likely due to observational filtering inherent to satellites.

From Figure 5, it can be seen that our momentum flux estimates have amplitudes in the order of 25–45 m^2/s^2. Some large amplitudes of about 90 m^2/s^2 can be observed above 96 km of altitude, where the corresponding statistical uncertainties are in the order of 10% or more (see bottom panels). Both momentum flux estimates exhibit variability in time and height, although it is more evident in the case of <u'w'>. Notice that despite the 28-day averaging, the magnitudes of <u'w'> and <v'w'> are considerable throughout the entire period of time analyzed in this study. Momentum flux estimates averaged over 20 days presented by Placke et al. (2015) exhibit maximum amplitudes of 6–8 m^2/s^2 during the summer of the Northern Hemisphere. The largest amplitudes of 10-day momentum flux estimates shown by Spargo et al. (2019) reach values of 30–40 m^2/s^2 in the beginning of the spring of the Southern Hemisphere. On the other hand, de Wit et al. (2017) observed monthly mean momentum fluxes over Tierra del Fuego with amplitudes larger than 70 m^2/s^2 during the summer. These amplitude values are in the same order as those obtained in our study. Hence, it is clear that the wave activity in the MLT region over the Patagonian sector is very strong. This is also consistent with previous studies based on satellite measurements (e.g., Ern et al., 2011), and numerical simulations (e.g., Lund et al., 2020).

As GWs propagate upwards, they transfer momentum and energy into the mean flow. Consequently, a decrease in the vertical flux of zonal momentum should correspond with an increase in the zonal wind speed (e.g., Fan et al., 1991). In other words, a decrease of the momentum flux indicates that a wave drag has been introduced into the mean flow, thus triggering an acceleration of the zonal wind. Our results are consistent with this reasoning, since for altitudes below 90–92 km, <u'w'> amplitudes, which are mostly positive, exhibit a clear vertical gradient: as the altitude increases, they progressively decrease from values of around 70–75 m^2/s^2 below 82 km, to values of ~10 m^2/s^2 above 90 km. The latter is also consistent with the results on u_z presented in the previous section. Besides, note that after February 22, negative values of <u'w'> start to develop below 90–91 km. At that time of the year, U has become eastward at all altitudes observed by SIMONe, a condition that allows westward propagating GWs to reach higher altitudes and, most likely, induce the aforementioned <u'w'> negative values.

In the case of <v'w'>, an upward movement of southward momentum dominates mostly below ~91 km, from the beginning of October until the end of March. During the last week of December 2019, positive values of <v'w'> start to dominate above 92–94 km, an altitude range that had been dominated by negative values of <v'w'> since the beginning of November 2019. During the latter, and approximately above 96 km of altitude, an upward movement of eastward momentum can be noticed again. These positive values of <u'w'> develop very abruptly around November 26, and remain dominant above 96 km for more than 25 days. We wonder if this might be an indicative of eastward momentum deposition by GWs that were in situ generated at altitudes above 90 km.

Momentum flux estimates obtained after subtracting the mean winds determined with the homogeneous method were also analyzed (not shown). In this case, only the 4-h, 8-km mean horizontal winds are used to determine $\hat{f}$ (see Equation 5). These momentum flux estimates have similar amplitudes to those presented in Figure 5. However, they exhibit some differences in their variability in time and altitude, and their statistical uncertainties are larger than those shown in Figure 5. It is for the latter and for consistency reasons, that the present study has been focused on analyzing the momentum fluxes that result from subtracting the mean horizontal and vertical winds obtained after applying the gradient method.

To finalize, we discuss the procedure followed to estimate σ(u'w') and σ(v'w'), and the reason for calculating 28-day averages. Unless one knows with some degree of certainty that a given wave event has occurred, the effects of GWs should be treated as stochastic processes. In other words, the mean momentum flux estimates are highly dependent on the effects of geophysical variability. Kudeki and Franke (1998) showed that in order to obtain statistically significant momentum flux estimates at mesospheric heights, one must consider averaging intervals of more than 25 days. Specifically, they found that the statistical uncertainty of <u'w'> can be approximated with:

$$\sigma(u'w') = \sqrt{\frac{(< u'u' >)(< w'w' >)}{T \, / \, \tau}}, \tag{6}$$

where, <u'u'> and <w'w'> are averaged over the interval of time *T*; and τ is equal to half of the mesosphere Brunt-Väisälä period (~7 min). σ(v'w') is obtained using same Equation 6, but replacing <u'u'> by <v'v'>. Selection of an averaging window *T* = 28 days resulted in the values presented in Figure 5. In this way, the <u'w'> and <v'w'> obtained from our study must be understood as representatives of a monthly mean momentum flux due to waves with periods of 4 h or less, and horizontal scales less than 400 km. Besides, for those estimates corresponding to altitudes lower than ~98 km, statistical uncertainties between 2 and 15–16 m²/s² should be taken into consideration.

The momentum flux estimates are also affected by the correlated Doppler shift errors. In other words, because the Doppler shift uncertainties are squared when introduced into Equation 4, the resulting momentum flux estimates are in fact an overestimation of the real <u'w'> and <v'w'> (Vierinen et al., 2019). However, given that the error propagated Doppler shift uncertainties we obtained are small (~1 order of magnitude smaller than the statistical uncertainties) and that the amplitudes of <u'w'> and <v'w'> are large, the effects of the correlated errors were neglected in this study. We plan to further investigate this issue by extending our analysis to include non-zero lag second-order statistics of the wind velocities.

5. Concluding Remarks

The first multistatic meteor radar based studies of mean winds, tides, gradients, and momentum flux over the southern part of Patagonia have been presented in this paper. By doing this, we have demonstrated the ability of SIMONe Argentina to obtain not only information on typical MLT parameters such as mean winds and tides, but also to successfully estimate previously little investigated parameters, such as horizontal and vertical gradients of the horizontal winds. Using the latter, one can estimate, for example, the horizontal divergence and the relative vorticity, parameters from which global circulation models can benefit and in this way help to further the understanding of MLT dynamics.

Our results show a strong positive vertical gradient in the zonal wind during the summer, in agreement with the residual mean meridional circulation. Besides, the northward zonal gradient (u_y) is stronger than the eastward zonal gradient (u_x), which indicates latitudinal changes of the zonal wind most likely due to the influence of the Southern Hemisphere polar vortex. Mean vertical winds (w_0) have also been estimated, but only when the horizontal and vertical gradients were taken into account.

Momentum fluxes, <u'w'> and <v'w'>, have been estimated after removal of horizontal and vertical mean winds that were fitted together with the horizontal wind gradients. Compared to some previous studies, our momentum flux estimates exhibit larger amplitudes, which indicates that the GW activity in the MLT over southern Patagonia is very strong. The statistical uncertainties of <u'w'> and <v'w'> were also included in the analysis. The latter revealed that in order to have statistically significant momentum flux estimates, one should consider averages of at least 28 days. In this way, our results must be considered as representative of monthly mean momentum fluxes, driven by waves with periods shorter than 4 h, vertical wavelengths shorter than 8 km, and horizontal scales less than 400 km.

We are confident that SIMONe Argentina has also the potential to investigate non-zero lag second-order statistics of MLT wind velocities, for example, by using correlation function techniques such as those presented in Vierinen et al. (2019). This will be explored in future studies. Besides, we also plan to investigate momentum flux estimates without averaging over long periods of time, provided there is evidence of specific (deterministic) wave events occurring in the troposphere/stratosphere.

Data Availability Statement

The data used to produce the figures is available in HDF5 format at DOI: 10.22000/342.

References

Andrews, D. G., Holton, J. R., & Leovy, C. B. (1987). *Middle atmosphere dynamics*. San Diego, CA: Academic Press. https://doi.org/10.1002/qj.49711548612

Andrioli, V. F., Batista, P. P., Clemesha, B. R., Schuch, N. J., & Buriti, R. A. (2015). Multi-year observations of gravity wave momentum fluxes at low and middle latitudes inferred by all-sky meteor radar. *Annales Geophysicae*, *33*, 1183–1193. https://doi.org/10.5194/angeo-33-1183-2015

Andrioli, V. F., Fritts, D. C., Batista, P. P., & Clemesha, B. R. (2013). Improved analysis of all-sky meteor radar measurements of gravity wave variances and momentum fluxes. *Annales Geophysicae*, *31*, 889–908. https://doi.org/10.5194/angeo-31-889-2013

Babu, V. S., Ramkumar, G., & John, S. R. (2012). Seasonal variation of planetary wave momentum flux and the forcing towards mean flow acceleration in the MLT region. *Journal of Atmospheric and Solar-Terrestrial Physics*, *78–79*, 53–61. https://doi.org/10.1016/j.jastp.2011.05.010

Browning, K. A., & Wexler, R. (1968). The determination of kinematic properties of a wind field using Doppler radar. *Journal of Applied Meteorology*, *7*(1), 105–113.

Burnside, R. G., Herrero, F. A., Meriwether, J. W., & Walker, J. C. G. (1981). Optical observations of thermospheric dynamics at Arecibo. *Journal of Geophysical Research*, *86*, 5532–5540.

Charuvil Asokan, H., Chau, J. L., Marino, R., Vierinen, J., Vargas, F., Urco, J. M., et al. (2020). Study of second-order wind statistics in the mesosphere and lower thermosphere region from multistatic specular meteor radar observations during the SIMONe 2018 campaign. *Atmospheric Chemistry and Physics*. https://doi.org/10.5194/acp-2020-974

Chau, J. L., Hoffmann, P., Pedatella, N. M., Matthias, V., & Stober, G. (2015). Upper mesospheric lunar tides over middle and high latitudes during sudden stratospheric warming events. *Journal of Geophysical Research: Space Physics*, *120*(4), 3084–3096. https://doi.org/10.1002/2015JA020998

Chau, J. L., Stober, G., Hall, C. M., Tsutsumi, M., Laskar, F. I., & Hoffmann, P. (2017). Polar mesospheric horizontal divergence and relative vorticity measurements using multiple specular meteor radars. *Radio Science*, *52*, 811–828. https://doi.org/10.1002/2016RS006225

Chau, J. L., Urco, J. M., Vierinen, J., Harding, B. J., Clahsen, M., Pfeffer, N., et al. (2020). Multistatic specular meteor radar network in Peru: System description and initial results. *Earth and Space Science*, *8*(1), e2020EA001293. https://doi.org/10.1002/essoar.10503328.1

Chau, J. L., Urco, J. M., Vierinen, J. P., Volz, R. A., Clahsen, M., Pfeffer, N., & Trautner, J. (2019). Novel specular meteor radar systems using coherent MIMO techniques to study the mesosphere and lower thermosphere. *Atmospheric Measurement Techniques*, *12*(4), 2113–2127. https://doi.org/10.5194/amt-12-2113-2019

Clemesha, B. R., Batista, P. P., Buriti da Costa, R. A., & Schuch, N. (2009). Seasonal variations in gravity wave activity at three locations in Brazil. *Annales Geophysicae*, *27*, 1059–1065. https://doi.org/10.5194/angeo-27-1059-2009

Conde, M., & Smith, R. W. (1998). Spatial structure in the thermospheric horizontal wind above Poker Flat, Alaska, during solar minimum. *Journal of Geophysical Research*, *103*, 9449–9472. https://doi.org/10.1029/97JA03331

Conte, J. F., Chau, J. L., Laskar, F. I., Stober, G., Schmidt, H., & Brown, P. (2018). Semidiurnal solar tide differences between fall and spring transition times in the Northern Hemisphere. *Annales Geophysicae*, *36*, 999–1008. https://doi.org/10.5194/angeo-36-999-2018

Conte, J. F., Chau, J. L., & Peters, D. H. W. (2019). Middle- and high-latitude mesosphere and lower thermosphere mean winds and tides in response to strong polar-night jet oscillations. *Journal of Geophysical Research*, *124*, 9262–9276. https://doi.org/10.1029/2019JD030828

Conte, J. F., Chau, J. L., Stober, G., Pedatella, N., Maute, A., Hoffmann, P., et al. (2017). Climatology of semidiurnal lunar and solar tides at middle and high latitudes: Interhemispheric comparison. *Journal of Geophysical Research: Space Physics*, *122*(7), 7750–7760. https://doi.org/10.1002/2017JA024396

de Wit, R. J., Janches, D., Fritts, D. C., & Hibbins, R. E. (2016). QBO modulation of the mesopause gravity wave momentum flux over Tierra del Fuego. *Geophysical Research Letters*, *43*, 4049–4055. https://doi.org/10.1002/2016GL068599

de Wit, R. J., Janches, D., Fritts, D. C., Stockwell, R. G., & Coy, L. (2017). Unexpected climatological behavior of MLT gravity wave momentum flux in the lee of the Southern Andes hot spot. *Geophysical Research Letters*, *44*, 1182–1191. https://doi.org/10.1002/2016GL072311

Egito, F., Andrioli, V. F., & Batista, P. P. (2016). Vertical winds and momentum fluxes due to equatorial planetary scale waves using all-sky meteor radar over Brazilian region. *Journal of Atmospheric and Solar-Terrestrial Physics*, *149*, 108–119. https://doi.org/10.1016/j.jastp.2016.10.005

Ern, M., Preusse, P., Gille, J. C., Hepplewhite, C. L., Mlynczak, M. G., Russell, J. M., III, & Riese, M. (2011). Implications for atmospheric dynamics derived from global observations of gravity wave momentum flux in stratosphere and mesosphere. *Journal of Geophysical Research*, *116*. https://doi.org/10.1029/2011JD015821

Fan, Y., Klostermeyer, J., & Rüster, R. (1991). VHF radar observation of gravity wave critical levels in the mid-latitude summer mesopause region. *Geophysical Research Letters*, *18*, 697–700.

Forbes, J. M. (1984). Middle atmosphere tides. *Journal of Atmospheric and Terrestrial Physics*(46), 1049–1067.

Fritts, D. C. (1984). Gravity wave saturation in the middle atmosphere: A review of theory and observations. *Reviews of Geophysics*, *22*, 275–308.

Fritts, D. C., & Alexander, M. J. (2003). Gravity wave dynamics and effects in the middle atmosphere. *Reviews of Geophysics*, *41*(1), 1003. https://doi.org/10.1029/2001RG000106

Fritts, D. C., Hoppe, U.-P., & Inhester, B. (1990). A study of the vertical motion field near the high-latitude summer mesopause during MAC/SINE. *Journal of Atmospheric and Terrestrial Physics*, *52*, 927–938.

Fritts, D. C., Iimura, H., Lieberman, R., Janches, D., & Singer, W. (2012). A conjugate study of mean winds and planetary waves employing enhanced meteor radars at Rio Grande, Argentina (53.8°S) and Juliusruh, Germany (54.6°N). *Journal of Geophysical Research*, *117*. https://doi.org/10.1029/2011JD016305

Fritts, D. C., Janches, D., & Hocking, W. K. (2010). Southern Argentina Agile Meteor Radar: Initial assessment of gravity wave momentum fluxes. *Journal of Geophysical Research*, *115*. https://doi.org/10.1029/2010JD013891

Fritts, D. C., Janches, D., Hocking, W. K., Mitchell, N. J., & Taylor, M. J. (2012). Assessment of gravity wave momentum flux measurement capabilities by meteor radars having different transmitter power and antenna configurations. *Journal of Geophysical Research*, *117*(D10108). https://doi.org/10.1029/2011JD017174

He, M., Chau, J. L., Stober, G., Hall, C. M., Tsutsumi, M., & Hoffmann, P. (2017). Application of Manley-Rowe relation in analyzing nonlinear interactions between planetary waves and the solar semidiurnal tide during 2009 sudden stratospheric warming event. *Journal of Geophysical Research: Space Physics*, *122*(10), 783–810. https://doi.org/10.1002/2017JA024630

Hines, C. O. (1988). A modeling of atmospheric gravity waves and wave drag generated by isotropic and anisotropic terrain. *Journal of the Atmospheric Sciences*, *45*, 309–322.

Hocking, W. K. (2005). A new approach to momentum flux determinations using SKiYMET meteor radars. *Annales Geophysicae*, *23*(7), 2433–2439. https://doi.org/10.5194/angeo-23-2433-2005

Hocking, W. K., Fuller, B., & Vandepeer, B. (2001). Real-time determination of meteor-related parameters utilizing modern digital technology. *Journal of Atmospheric and Solar-Terrestrial Physics*, *63*, 155–169. https://doi.org/10.1016/S1364-6826(00)00138-3

Hocking, W. K., & Thayaparan, T. (1997). Simultaneous and collocated observations of winds and tides by MF and meteor radars over London, Canada (43°N, 81°W), during 1994–1996. *Radio Science*, *32*(2), 833–865.

Hoffmann, P., Becker, E., Singer, W., & Placke, M. (2010). Seasonal variation of mesospheric waves at northern middle and high latitudes. *Journal of Atmospheric and Solar-Terrestrial Physics*, *72*(14–15), 1068–1079. https://doi.org/10.1016/j.jastp.2010.07.002

Holdsworth, D. A., Reid, I. M., & Cervera, M. A. (2004). Buckland Park all-sky interferometric meteor radar. *Radio Science*, *39*(5). https://doi.org/10.1029/2003RS003014

Jacobi, C., Portnyagin, Y. I., Solovjova, T. V., Hoffmann, P., Singer, W., Fahrutdinova, A. N., et al. (1999). Climatology of the semidiurnal tide at 52–56°N from ground-based radar wind measurements 1985–1995. *Journal of Atmospheric and Solar-Terrestrial Physics*, *61*(13), 975–991. https://doi.org/10.1016/S1364-6826(99)00065-6

Jia, M., Xue, X., Gu, S., Chen, T., Ning, B., Wu, J., et al. (2018). Multiyear observations of gravity wave momentum fluxes in the midlatitude mesosphere and lower thermosphere region by meteor radar. *Journal of Geophysical Research: Space Physics*, *123*, 5684–5703. https://doi.org/10.1029/2018JA025285

Jones, J., Webster, A. R., & Hocking, W. K. (1998). An improved interferometer design for use with meteor radars. *Radio Science*, *33*, 55–65. https://doi.org/10.1029/97RS03050

Kudeki, E., & Franke, S. J. (1998). Statistics of momentum flux estimation. *Journal of Atmospheric and Solar-Terrestrial Physics*, *60*, 1549–1553.

Kumar, K. K., Subrahmanyam, K. V., Mathew, S. S., Koushik, N., & Ramkumar, G. (2018). Simultaneous observations of the quasi 2-day wave climatology over the low and equatorial latitudes in the mesosphere lower thermosphere. *Climate Dynamics*, *51*, 221–233. https://doi.org/10.1007/s00382-017-3916-2

Laskar, F. I., Chau, J. L., Stober, G., Hoffmann, P., Hall, C. M., & Tsutsumi, M. (2016). Quasi-biennial oscillation modulation of the middle- and high-latitude mesospheric semidiurnal tides during August–September. *Journal of Geophysical Research: Space Physics*, *121*(5), 4869–4879. https://doi.org/10.1002/2015JA022065

Lindzen, R. S., & Chapman, S. (1969). Atmospheric tides. *Space Science Reviews*, *10*, 3–188.

Liu, A. Z., Lu, X., & Franke, S. J. (2013). Diurnal variation of gravity wave momentum flux and its forcing on the diurnal tide. *Journal of Geophysical Research: Atmospheres*, *118*, 1668–1678.

Liu, H.-L., & Roble, R. G. (2002). A study of a self-generated stratospheric sudden warming and its mesospheric-lower thermospheric impacts using the coupled TIME-GCM/CCM3. *Journal of Geophysical Research*, *107*, ACL151–ACL1518. https://doi.org/10.1029/2001JD001533

Lu, X., Chu, X., Li, H., Chen, C., Smith, J. A., & Vadas, S. L. (2017). Statistical characterization of high-to-medium frequency mesoscale gravity waves by lidar-measured vertical winds and temperatures in the MLT. *Journal of Atmospheric and Solar-Terrestrial Physics*, *162*, 3–15. https://doi.org/10.1016/j.jastp.2016.10.009

Lund, T., Fritts, D., Kam, W., Laughman, B., & Liu, H.-L. (2020). Numerical simulation of mountain waves over the Southern Andes, Part 1: Mountain wave and secondary wave character, evolutions, and breaking. *Journal of the Atmospheric Sciences*, *77*(12), 4337–4356.

McCormack, J. P., Coy, L., & Singer, W. (2014). Intraseasonal and interannual variability of the quasi 2 day wave in the Northern Hemisphere summer mesosphere. *Journal of Geophysical Research: Atmospheres*, *119*, 2928–2946. https://doi.org/10.1002/2013JD020199

Meriwether, J., Faivre, M., Fesen, C., Sherwood, P., & Veliz, O. (2008). New results on equatorial thermospheric winds and the midnight temperature maximum. *Annales Geophysicae*, *26*, 447–466.

Murphy, D. J., Forbes, J. M., Walterscheid, R. L., Hagan, M. E., Avery, S. K., Aso, T., et al. (2006). A climatology of tides in the antarctic mesosphere and lower thermosphere. *Journal of Geophysical Research*, *111*. https://doi.org/10.1029/2005JD006803

Offermann, D., Hoffmann, P., Knieling, P., Koppmann, R., Oberheide, J., Riggin, D. M., et al. (2011). Quasi 2 day waves in the summer mesosphere: Triple structure of amplitudes and long-term development. *Journal of Geophysical Research*, *116*. https://doi.org/10.1029/2010JD015051

Orte, P. F., Wolfram, E., Salvador, J., Mizuno, A., Begue, N., Bencherif, H., et al. (2019). Analysis of a southern sub-polar short-term ozone variation event using a millimetre-wave radiometer. *Annales Geophysicae*, *37*, 613–629. https://doi.org/10.5194/angeo-37-613-2019

Pancheva, D., & Mukhtarov, P. (2011). Atmospheric tides and planetary waves: Recent progress based on SABER/TIMED temperature measurements (2002–2007). *Aeronomy of the Earth's atmosphere and ionosphere* (Vol. *2*, pp. 19–56). Dordrecht: Springer. https://doi.org/10.1007/978-94-007-0326-1_2

Piani, C., Durran, D., Alexander, M. J., & Holton, J. R. (2000). A numerical study of three-dimensional gravity waves triggered by deep tropical convection and their role in the dynamics of the QBO. *Journal of the Atmospheric Sciences*, *57*, 3689–3702. https://doi.org/10.1029/2019EA000570

Placke, M., Hoffmann, P., Becker, E., Jacobi, C., Singer, W., & Rapp, M. (2011). Gravity wave momentum fluxes in the MLT–Part II: Meteor radar investigations at high and midlatitudes in comparison with modeling studies. *Journal of Atmospheric and Solar-Terrestrial Physics*, *73*, 911–920. https://doi.org/10.1016/j.jastp.2010.05.007

Placke, M., Hoffmann, P., Latteck, R., & Rapp, M. (2015). Gravity wave momentum fluxes from MF and meteor radar measurements in the polar MLT region. *Journal of Geophysical Research: Space Physics*, *120*, 736–750. https://doi.org/10.1002/2014JA020460

Placke, M., Stober, G., & Jacobi, C. (2011). Gravity wave momentum fluxes in the MLT–Part I: Seasonal variation at Collm (51.3°N, 13.0°E). *Journal of Atmospheric and Solar-Terrestrial Physics*, *73*, 904–910. https://doi.org/10.1016/j.jastp.2010.05.007

Rossby, C.-G. (1939). Relation between variations in the intensity of the zonal circulation of the atmosphere and the displacements of the semipermanent centers of action. *Journal of Marine Research*, *2*, 38–55.

Sandford, D. J., Muller, H. G., & Mitchell, N. J. (2006). Observations of lunar tides in the mesosphere and lower thermosphere at Arctic and middle latitudes. *Atmospheric Chemistry and Physics*, *6*, 4117–4127.

Siddiqui, T. A., Maute, A., Pedatella, N., Yamazaki, Y., Lühr, H., & Stolle, C. (2018). On the variability of the semidiurnal solar and lunar tides of the equatorial electrojet during sudden stratospheric warmings. *Annales Geophysicae*, *36*, 1545–1562. https://doi.org/10.5194/angeo-2018-80

Smith, A. K. (2012). Global dynamics of the MLT. *Surveys in Geophysics*, *33*(6), 1177–1230.

Spargo, A. J., Reid, I. M., & MacKinnon, A. D. (2019). Multistatic meteor radar observations of gravity-wave–tidal interaction over southern Australia. *Atmospheric Measurement Techniques*, *12*, 4791–4812. https://doi.org/10.5194/amt-12-4791-2019

Stening, R. J., Forbes, J. M., Hagan, M. E., & Richmond, A. D. (1997). Experiments with a lunar atmospheric tidal model. *Journal of Geophysical Research*, *102*, 13465–13472. https://doi.org/10.1029/97JD00778

Stober, G., & Chau, J. L. (2015). A multistatic and multifrequency novel approach for specular meteor radars to improve wind measurements in the mlt region. *Radio Science*, *50*, 431–442. https://doi.org/10.1002/2014RS005591

Thorsen, D., Franke, S. J., & Kudeki, E. (1997). A new approach to MF radar interferometry for estimating mean winds and momentum flux. *Radio Science*, *32*(2), 707–726.

Trinh, Q. T., Ern, M., Doornbos, E., Preusse, P., & Riese, M. (2018). Characteristics of the quiet-time hot spot gravity waves observed by GOCE over the Southern Andes on 5 July 2010. *Annales Geophysicae*, *36*, 425–444. https://doi.org/10.5194/angeo-36-425-2018

Urco, J. M., Chau, J. L., Milla, M. A., Vierinen, J., & Weber, T. (2018). Coherent MIMO to improve aperture synthesis radar imaging of field-aligned irregularities: First results at Jicamarca. *IEEE Transactions on Geoscience and Remote Sensing*(99), 1–11. https://doi.org/10.1109/TGRS.2017.2788425

Urco, J. M., Chau, J. L., Weber, T., & Latteck, R. (2019). Enhancing the spatio-temporal features of polar mesosphere summer echoes using coherent MIMO and radar imaging at MAARSY. *Atmospheric Measurement Techniques*, *12*, 955–969. https://doi.org/10.5194/amt-12-955-2019

Vadas, S. L., & Becker, E. (2019). Numerical modeling of the generation of tertiary gravity waves in the mesosphere and thermosphere during strong mountain wave events over the Southern Andes. *Journal of Geophysical Research*, *124*, 7687–7718. https://doi.org/10.1029/2019JA026694

Vadas, S. L., Xu, S., Yue, J., Bossert, K., Becker, E., & Baumgarten, G. (2019). Characteristics of the quiet-time hot spot gravity waves observed by GOCE over the Southern Andes on 5 July 2010. *Journal of Geophysical Research: Space Physics*, *124*, 7034–7061. https://doi.org/10.1029/2019JA026693

Vierinen, J., Chau, J. L., Charuvil, H., Urco, J. M., Clahsen, M., Avsarkisov, V., et al. (2019). Observing mesospheric turbulence with specular meteor radars: A novel method for estimating second-order statistics of wind velocity. *Earth and Space Science*, *6*, 1171–1195. https://doi.org/10.1029/2019EA000570

Vierinen, J., Chau, J. L., Pfeffer, N., Clahsen, M., & Stober, G. (2016). Coded continuous wave meteor radar. *Atmospheric Measurement Techniques*, *9*(2), 829–839.

Vincent, R. A., Kovalam, S., Reid, I. M., & Younger, J. P. (2010). Gravity wave flux retrievals using meteor radars. *Geophysical Research Letters*, *37*. https://doi.org/10.1029/2010GL044086

Wilhelm, S., Stober, G., & Brown, P. (2019). Climatologies and long-term changes in mesospheric wind and wave measurements based on radar observations at high and mid latitudes. *Annales Geophysicae*, *37*, 851–875. https://doi.org/10.5194/angeo-37-851-2019

Yamazaki, Y., Matthias, V., Miyoshi, Y., Stolle, C., Siddiqui, T., Kervalishvili, G., et al. (2020). September 2019 antarctic sudden stratospheric warming: Quasi-6-day wave burst and ionospheric effects. *Geophysical Research Letters*, *47*. https://doi.org/10.1029/2019GL086577